Journal of Materials Chemistry A

ROYAL SOCIETY OF CHEMISTRY

PAPER

View Article Online
View Journal | View Issue

Cite this: J. Mater. Chem. A, 2023, 11, 8119

High thermoelectric and mechanical performance achieved by a hyperconverged electronic structure and low lattice thermal conductivity in GeTe through $CuInTe_2$ alloying†

Hyunji Kim, [a] Samuel Kimani Kihoi, [a] U. Sandhya Shenoy, [b] Joseph Ngugi Kahiu, [c] Dong Hyun Shin, [a] D. Krishna Bhat [d] and Ho Seong Lee *[a]

GeTe-based thermoelectric materials have a very high hole carrier concentration ($\sim 10^{21}$ cm^{-3}), and thus, improving the figure of merit, *ZT*, is substantially challenging. In this work, we foremost dope Bi to lower the majority carrier concentration, followed by alloying $CuInTe_2$ to further adjust the hole concentration to an optimal level (0.5–2.0 × 10^{20} cm^{-3}). This strategy also improves the structural symmetry and leads to hyperconverged valence sub-bands and resonance levels, increasing the effective mass from 1.42 m_0 to 1.95 m_0. Consequently, a high power factor of ~23 μW cm^{-1} K^{-2} at room temperature and ~41 μW cm^{-1} K^{-2} at 623 K in the $(Ge_{0.93}Bi_{0.05}Te_{0.98})(CuInTe_2)_{0.01}$ sample is reported. Moreover, the introduced point defects and nano-deposits reduce the lattice thermal conductivity to amorphous levels. As a result, the $(Ge_{0.93}Bi_{0.05}Te_{0.98})(CuInTe_2)_{0.01}$ sample has a peak *ZT* value of ~2.16 at 623 K and an average *ZT* value of ~1.42 at 300–773 K. A record high hardness value (~277 Hv) is achieved. Simultaneous Bi doping and $CuInTe_2$ alloying appear to be an effective strategy for increasing the *ZT* values of GeTe-based compounds.

Received 29th November 2022
Accepted 20th February 2023

DOI: 10.1039/d2ta09280h

rsc.li/materials-a

Introduction

Thermoelectric technology, which converts heat directly into electricity and *vice versa*, has attracted great attention as one of promising solutions to the energy crisis and environmental degradation, and various related studies have been reported recently.[1–6] To make thermoelectric technology more economical and expand its application range, the energy conversion efficiency, measured by the figure of merit (*ZT*), should be maximized. The dimensionless *ZT* is defined as $ZT = S^2\sigma T/\kappa_{total}$, where S, σ, T, and κ_{total} are the Seebeck coefficient, electrical conductivity, absolute temperature, and total thermal conductivity (the sum of lattice κ_{latt} and electronic κ_{ele} components), respectively.[7–9] For enhancing the *ZT* value, both a high power factor ($S^2\sigma$) and low lattice thermal conductivity (κ_{latt}) are simultaneously coveted. Improving the power factor is achieved through band convergence,[10,11] resonant levels,[12,13] the energy filtering effect,[14,15] and modulation doping.[16,17] On the other hand, minimizing the lattice thermal conductivity is attained through all-scale hierarchical phonon scattering,[18,19] nanoparticles,[20,21] and various defects.[6,22] So far, thermoelectric materials, such as Bi_2Te_3-based compounds,[23] chalcogenides,[24] SiGe,[25] half-Heusler,[26] Zintl phases compounds,[27] skutterudites,[28] *etc.*, have been investigated with combinations of the above-mentioned methods to improve thermoelectric performance.

GeTe is a chalcogenide thermoelectric material for mid-temperature application with a superior conversion efficiency.[8,29–34] Pristine GeTe undergoes a ferroelectric phase transition from a high-temperature cubic structure ($Fm\bar{3}m$) to low-temperature rhombohedral structure ($R3m$) near 700 K, accompanied by a Peierls-type distortion.[35] This broken inversion symmetry induces a change in the electron band structure and strong spin-orbital coupling (SOC).[30,36] First of all, the rhombohedral GeTe has 3 L and 1 Z pockets for light carrier valence bands, and 6 Σ and 6 η pockets for heavy carrier valence bands which merges into 4 L and 12 Σ pockets for light and heavy hole bands, respectively, when it undergoes the transition to cubic GeTe.[36,37] Secondly, the induced strong SOC results in the Rashba spin splitting, in which the original single band edge splits into two band extrema with opposite spin

[a]School of Materials Science and Engineering, Kyungpook National University, 80 Daehak-ro, Buk-gu, Daegu, 41566, Republic of Korea. E-mail: hs.lee@knu.ac.kr
[b]Department of Materials Science and Engineering, Institute of Engineering and Technology, Srinivas University, Mukka, 574146, Mangalore, Karnataka, India
[c]Department of Hydrogen and Renewable Energy, Kyungpook National University, 80 Daehak-ro, Buk-gu, Daegu, 41566, Republic of Korea
[d]Department of Chemistry, National Institute of Technology Karnataka, Surathkal, Srinivasnagar, 575025, Mangalore, Karnataka, India

† Electronic supplementary information (ESI) available. See DOI: https://doi.org/10.1039/d2ta09280h

momenta.[30,38] Pristine GeTe is also characterized by a high hole concentration due to the low formation energy of intrinsic Ge vacancies, leading to the degradation of the thermoelectric performance.[8]

Optimization of the hole concentration in GeTe is implemented by doping trivalent elements such as Bi,[34,39] Sb,[40,41] and In,[34,42] and suppressing the Ge vacancies.[43] Enhancement of the Seebeck coefficient has been achieved by several band engineering methods, including band convergence,[44] resonance state,[34] the Rashba effect.[30] and entropy engineering,[18,29,45] and alloying with other compounds such as $NaSbTe_2$,[32] $AgSbTe_2$,[46] $CuSbTe_2$,[47] and CdSe[32] has been employed to introduce an all-scale hierarchical phonon scattering as well as band engineering. In addition, studies have been reported that showed a synergistic improvement in thermoelectric properties by simultaneous doping with effective dopants such as Cu and In,[48] Sn and Sb,[30] and Cu and Sb.[49]

$CuInTe_2$, a ternary I-III-VI_2 compound, is a medium-temperature thermoelectric material with a low carrier concentration ($\sim 10^{18}$ cm^{-3}).[50] This compound also has a tetragonal crystal structure, a quasi-cubic structure in which two sphalerites are stacked in the *c*-axis, so that it has a similar crystal structure to cubic GeTe.[51] In this study, we fabricate $(Ge_{1-x-2y}Bi_xTe_{1-2y})(CuInTe_2)_y$ ($x = 0$, 0.05; $y = 0$, 0.005, 0.01, 0.02, and 0.03) to reduce the high carrier concentration of GeTe by doping with trivalent Bi, and alloy it with a $CuInTe_2$ compound to further adjust the carrier concentration and electrical structure. As a result, the carrier concentration is maintained at an optimum level. Moreover, a large DOS distortion due to the hyperconverged valence sub-band and the resonance level induced near the Fermi level is confirmed through DFT calculations. This distorted DOS increases the effective mass from 1.42 m_0 to 1.95 m_0, leading to an increase in the Seebeck coefficient. Thus, a very high power factor of ~23 μW cm^{-1} K^{-2} at room temperature and ~41 μW cm^{-1} K^{-2} at 623 K is obtained in the $(Ge_{0.93}Bi_{0.05}Te_{0.98})(CuInTe_2)_{0.01}$ sample. Furthermore, the lattice thermal conductivity decreases due to the influence of the $CuInTe_2$ nanoprecipitate and point defects introduced by the dopants. As a result, the $(Ge_{0.93}Bi_{0.05}Te_{0.98})(CuInTe_2)_{0.01}$ sample has a peak *ZT* value of ~2.16 at 623 K and an average *ZT* value of ~1.42 at 300–773 K, showing high thermoelectric properties. The $(Ge_{0.91}Bi_{0.05}Te_{0.96})(CuInTe_2)_{0.02}$ sample showed very high mechanical stability with a record high hardness value of 277 Hv.

Experimental details

Reagents

Alfa Aesar's Ge (pieces, 99.999%), Te (broken ingot, 99.99%), Cu powder (powder, 99.9%), In (shot, 99.99%), and Bi (shot, 99.999%) were used for synthesis without any further purification.

Sample synthesis

Samples (~16 g) of $(Ge_{1-x-2y}Bi_xTe_{1-2y})(CuInTe_2)_y$ ($x = 0$, 0.05; $y = 0$, 0.005, 0.01, 0.02, and 0.03) were weighed according to their stoichiometric ratio and loaded in quartz tubes. The tubes were vacuumed to 10^{-3} Torr, purged with Ar gas three times then sealed under a vacuum pressure of 10^{-3} Torr. These sealed ampoules were slowly heated to 1223 K for 12 h in a rocking furnace and then kept at this temperature for 6 h. Subsequently, the ampoules were quenched in water, annealed in a box furnace at 923 K for 3 days and then slowly cooled down to room temperature. Next, the obtained ingots were ground to below 45 μm and then sintered using a hot press under a uniaxial pressure of 100 MPa at 823 K for 1 h under an Ar atmosphere. The pellets were cut into the required shapes by using a diamond wire saw for various analysis processes.

Characterization

X-ray diffraction data were obtained by using a Panalytical EMPYREAN X-ray diffractometer with Cu Kα radiation (λ = 1.5425 Å), scanning from 20° to 80° with a 0.02° step at room temperature. The microstructure and chemical composition were characterized on a Hitachi SU8230 field emission scanning electron microscopy (FE-SEM) instrument with an OXFORD Ultim Max100 energy dispersive X-ray spectrometer (EDS). The chemical composition of the samples was also determined using a JEOL JXA-8530F field emission electron probe micro analyzer (FE-EPMA) at 15 kV in combination with wavelength dispersive spectroscopy (WDS) on the polished surfaces. The microstructure and atomic defects were investigated using a Titan G2 ChemSTEM Cs probe field emission transmission electron microscope (FE-TEM) operating at 200 kV. The sample preparation for FE-TEM was performed using a Hitachi NX5000 focused ion beam (FIB). The microhardness of the samples was measured using the Vickers hardness method with a Emcotest universal hardness tester (DuraScan-20-G5, Australia).

Thermoelectric measurement

Temperature-dependent resistivity and Seebeck coefficient were measured from ambient temperature to 773 K using a ULVAC ZEM-3 instrument with an error of 8%. The total thermal conductivity was calculated based on $\kappa_{total} = D \times C_p \times \rho$, where D, C_p, and ρ are the thermal diffusivity, specific heat capacity, and density, respectively. The thermal diffusivity was measured using an ULVAC TC-9000H instrument with an error of 8%. The electronic thermal conductivity is calculated using the Wiedmann–Franz relation $\kappa_{ele} = \sigma \times L \times T$, where σ, L, and T are the electrical conductivity, Lorenz number, and absolute temperature, respectively. The Lorenz number is determined by $L = 1.5 + \exp[-|S|/116]$, where S and L have the units of μV K^{-1} and 10^{-8} WΩ K^{-2}, respectively.[52] The lattice thermal conductivity is obtained by subtracting the electronic thermal conductivity from the total thermal conductivity. The specific heat capacity was derived by using the Dulong–Petit law ($C_p = 3R/M$) where R and M are the gas constant and molecular mass per mole, respectively. The density was obtained using Archimedes' method. The Hall effect measurement was carried out using an Ecopia HMS-3000H by the van der Pauw method under a reversible 0.55 T magnetic field to determine the carrier concentration and mobility at room temperature.

Computational technique

Density functional theory calculations were carried out using the Quantum ESPRESSO package.[53] A generalized gradient approximation functional and the Perdew, Burke and Erzenhoff (PBE) pseudopotential was used.[54] A $\sqrt{2} \times \sqrt{2} \times 2$ supercell was used to study the doped and pristine systems of cubic GeTe. For rhombohedral systems, a $2 \times 2 \times 2$ supercell was chosen. Fully relativistic pseudopotentials which considered $4s^2 4p^2$, $4d^{10} 5s^2 5p^4$, $3d^{10} 4s^1$, $5d^{10} 6s^2 6p^3$ and $4d^{10} 5s^2 5p^1$ as valence electrons of Ge, Te, Cu, Bi and In were used for the simulations. A cutoff energy of 50 R_y and a charge density of 400 R_y were chosen. Electronic structures of the relaxed supercells were determined along the respective high symmetry paths in the Brillouin zone for cubic and rhombohedral systems.

Results and discussion

To identify the crystal structure and the composing phase of the sintered $(Ge_{1-x-2y}Bi_xTe_{1-2y})(CuInTe_2)_y$ ($x = 0$, 0.05; $y = 0$, 0.005, 0.01, 0.02, and 0.03), X-ray diffraction (XRD) was conducted, and the results are shown in Fig. 1a. All peaks of pristine GeTe are indexed to the rhombohedral structure (PDF#47-1079, $R3m$ space group). After Bi doping, weak peaks at 27.3° and 45.3° additionally appear, which are indexed to pure Ge precipitates (PDF#65-9209). The excess Ge is precipitated due to the low formation energy of Ge vacancies (V''_{Ge}).[34,55–57] With increasing y, $CuInTe_2$ compounds (PDF#81-1937, $I\bar{4}2d$ space group) are observed as the secondary phase. Fig. 1b shows that as the content of dopants increases, the two peaks belonging to the (024) and (220) planes become closer. This is due to the relaxation of the structure along the <111> direction after alloying, making it conform to the cubic GeTe (PDF#52-0849, $Fm\bar{3}m$ space group).[34,58]

The calculated lattice parameters of $(Ge_{1-x-2y}Bi_xTe_{1-2y})(CuInTe_2)_y$ increase along the a and b axes and decrease along the c axis, as shown in Fig. 1c and Table S1.† The lattice parameters of pristine GeTe ($a = b = 4.169$ Å and $c = 10.661$ Å) compared to those of $(Ge_{0.89}Bi_{0.05}Te_{0.94})(CuInTe_2)_{0.03}$ ($a = b = 4.201$ Å and $c = 10.577$ Å) are shown. This change can be attributed to the bigger ionic radius of Cu^+ (0.96 Å), In^{3+} (0.81 Å), and Bi^{3+} (0.96 Å) in contrast to that of Ge^{2+} (0.73 Å). The expansion along the a and b axes and the contraction along the c axis of the rhombohedral structure imply a transition toward the cubic structure, which can also be confirmed with a refined lattice constant (a_1) and interaxial angle (α_1) based on a pseudo-cubic unit cell (Fig. 1d and Table S1†). After Bi doping, a_1 and α_1 increase simultaneously. With increasing y, a_1 is maintained at ~5.998 Å and α_1 gradually increases and gets close to ~89°. It is confirmed that the structural symmetry of alloyed GeTe is improved compared to that of the pristine sample.[55,59] This increased structural symmetry from $R3m$ to $Fm\bar{3}m$ induces

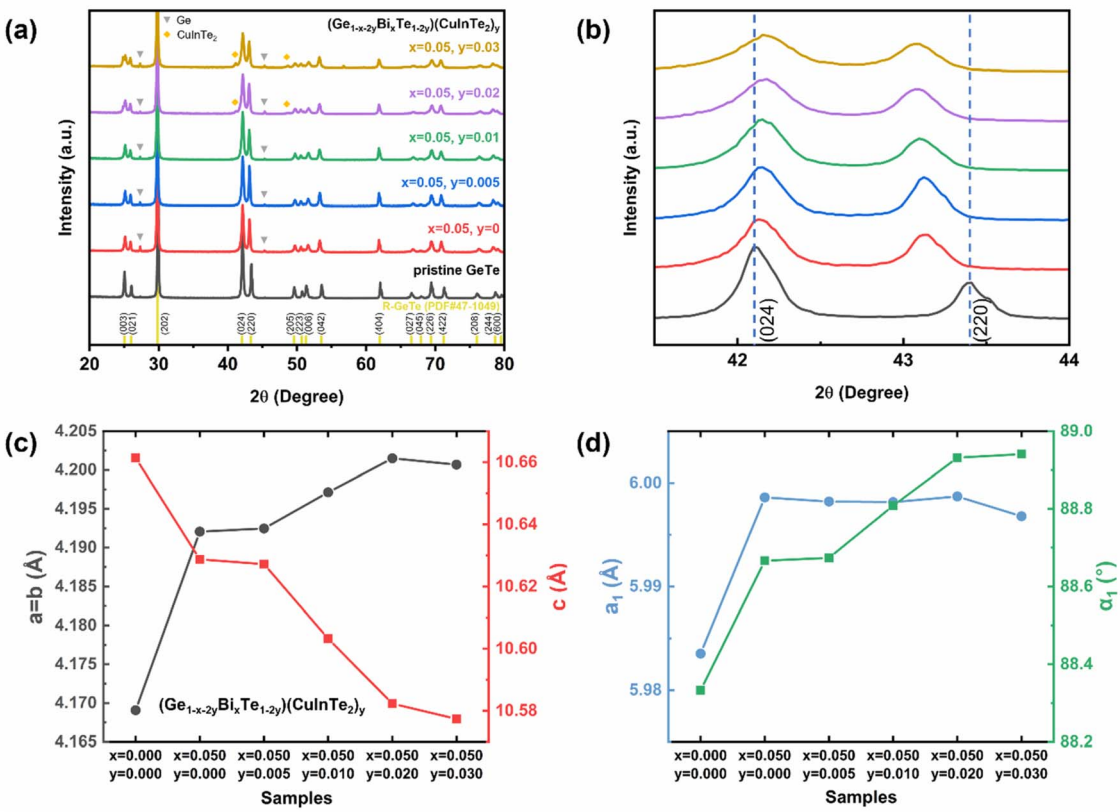

Fig. 1 (a) XRD patterns of $(Ge_{1-x-2y}Bi_xTe_{1-2y})(CuInTe_2)_y$ ($x = 0$ and 0.05; $y = 0.005$, 0.01, 0.02, and 0.03) samples. (b) Enlarged diffraction peaks of (024) and (220) in (a). (c) Experimental lattice parameters of $(Ge_{1-x-2y}Bi_xTe_{1-2y})(CuInTe_2)_y$. (d) The refined lattice parameter and interaxial angle based on a pseudo cubic unit cell.

Table 1 Nominal composition and EPMA analyzed composition of the matrix of the sample

Samples	Nominal composition (at%)	EPMA analyzed composition (at%)
$Ge_{0.95}Bi_{0.05}Te$	$Ge_{47.5}Bi_{2.5}Te_{50}$	$Ge_{47.93}Bi_{2.97}Te_{49.10}$
$(Ge_{0.93}Bi_{0.05}Te_{0.98})(CuInTe_2)_{0.01}$	$Ge_{46.5}Bi_{2.5}Cu_{0.5}In_{0.5}Te_{50}$	$Ge_{47}Bi_{2.52}Cu_{0.57}In_{0.57}Te_{49.34}$
$(Ge_{0.89}Bi_{0.05}Te_{0.94})(CuInTe_2)_{0.03}$	$Ge_{44.5}Bi_{2.5}Cu_{1.5}In_{1.5}Te_{50}$	$Ge_{44.45}Bi_{2.40}Cu_{1.73}In_{1.39}Te_{50.04}$

additional valence band convergence, contributing to the increase in the Seebeck coefficient,[8,60] which will be discussed later.

The SEM image of the fracture surface of pristine GeTe is displayed in Fig. S1,† clearly showing a herringbone structure, which is a typical morphological characteristic of GeTe.[61–63] Fig. S2† illustrates the SEM images and corresponding EDS mapping from the fracture surface. Fig. S2a† shows that the dark contrast phases in the SEM image are identified as Ge precipitates in the $(Ge_{0.93}Bi_{0.05}Te_{0.98})(CuInTe_2)_{0.01}$ sample. In Fig. S2b,† Cu and In are observed to be distributed in almost the same region in the $(Ge_{0.89}Bi_{0.05}Te_{0.94})(CuInTe_2)_{0.03}$ sample, and the $CuInTe_2$ compound, which is also confirmed by XRD, is observed to be located around the grain boundary.

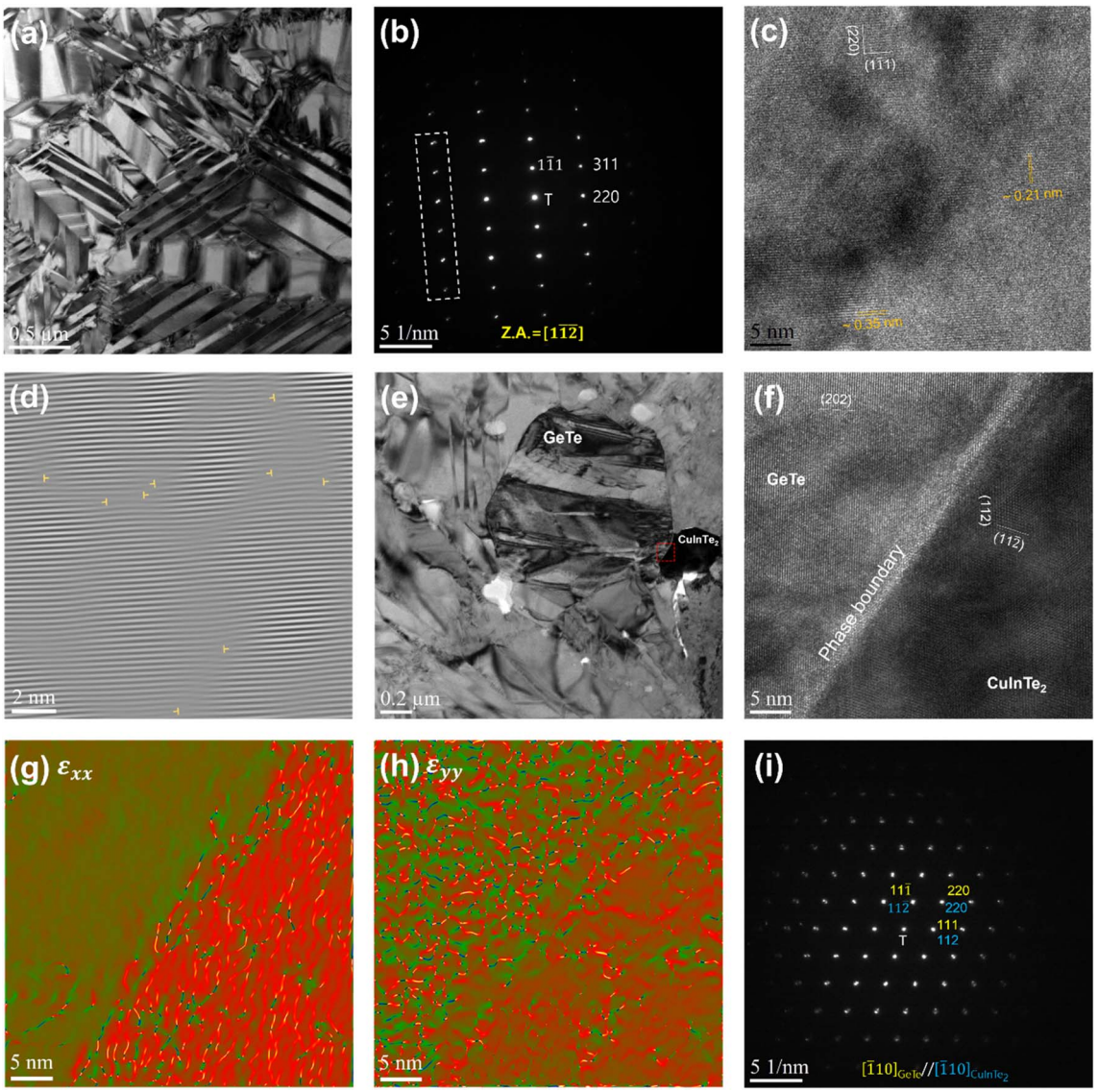

Fig. 2 Microstructure observation in the $(Ge_{0.93}Bi_{0.05}Te_{0.98})(CuInTe_2)_{0.01}$ sample. (a) Bright-field TEM micrograph, showing the herringbone structures. (b) SAED pattern of rhombohedral GeTe along the [1$\bar{1}$2] zone axis and the (c) corresponding HRTEM micrograph. (d) Inverse FFT image showing dislocations. (e) Bright-field TEM micrograph, showing a GeTe matrix grain and dark $CuInTe_2$ precipitate. (f) HRTEM micrograph of the red-square area in (e). GPA mappings from (c) along the (g) horizontal (ε_{xx}) and (h) vertical (ε_{yy}) directions. (i) SAED pattern with GeTe and the $CuInTe_2$ precipitate along the parallel zone axes.

We performed quantitative analysis using EPMA to accurately verify the composition of the samples, and the results of point analysis are shown in Table 1. The EPMA results of the analyzed samples were reasonable compared to the nominal composition. In the matrices of $(Ge_{0.93}Bi_{0.05}Te_{0.98})(CuInTe_2)_{0.01}$ and $(Ge_{0.89}Bi_{0.05}Te_{0.94})(CuInTe_2)_{0.03}$, Cu and In not involved in the formation of $CuInTe_2$ precipitates are evenly distributed. The results of the line scan between the matrix and precipitate at $(Ge_{0.89}Bi_{0.05}Te_{0.94})(CuInTe_2)_{0.03}$ are shown in Fig. S3.† The composition of the precipitate was ~28.26 at% Cu, ~21.92 at% In, and ~42.77 at% Te, which was confirmed to be the $CuInTe_2$ precipitate. This concurs well with the XRD results that $CuInTe_2$ precipitates exist in the matrix. The small amount of Ge detected in the $CuInTe_2$ precipitate is the Ge that is in the matrix beneath the $CuInTe_2$ precipitate.

To deeply understand the resulting microstructure of the $(Ge_{0.93}Bi_{0.05}Te_{0.98})(CuInTe_2)_{0.01}$ sample, we implemented field-emission transmission electron microscopy (FE-TEM). Fig. 2a shows a low-magnification bright-field TEM microscopy image, obviously exhibiting several herringbone structures composed of many domains and colonies.[63] This structure is manifested by the disruption of Friedel's symmetry in the rhombohedral structure.[63,64] The selected area electron diffraction (SAED) pattern along the $[1\bar{1}2]$ zone axis is shown in Fig. 2b, where there are split spots away from the transmitted beam (T), which are attributed to the neighbouring domains. The corresponding high-resolution TEM (HRTEM) micrograph in Fig. 2b identifies the interplanar distances as ~0.21 nm and ~0.35 nm, respectively, corresponding to the (220) and $(1\bar{1}1)$ planes. Fig. 2d indicates the occurrence of dislocations distributed through the inverse fast Fourier transformation (FFT) image in Fig. 2c. TEM-EDS analysis, depicted in Fig. S4,† revealed that Fig. 2e shows a GeTe matrix and dark-contrast $CuInTe_2$ precipitates on the right. Fig. S5b† shows the contrast-adjusted image for accurate identification of the $CuInTe_2$ precipitate. Fig. 2f shows the corresponding HRTEM micrograph of the red-square area in Fig. 2e, depicting the phase boundary between the GeTe matrix and $CuInTe_2$ precipitate. The geometric phase analysis (GPA) is performed to investigate the strain distribution of the GeTe matrix and $CuInTe_2$ precipitate.[65,66] The $CuInTe_2$ precipitate appears to be characterized by a relatively higher ε_{xx} (horizontal axis) and ε_{yy} (vertical axis) than the GeTe matrix, as shown in Fig. 2g and h. Such a nanoprecipitate with a difference in strain from the matrix, strong point defects, *etc.* interrupts the movement of phonons, which are the heat carriers, and contribute to the reduction of κ_{latt}. In addition, as shown in Fig. 2i, the presence of $CuInTe_2$ is confirmed once again in the SAED pattern showing the parallel crystal orientation relationship between the GeTe matrix and $CuInTe_2$ precipitate. It can be observed that the reflected spots spread around the transmitted beam. This is due to the small difference in the lattice parameter between the GeTe matrix and $CuInTe_2$ precipitate, which is illustrated with the schematic diagram in Fig. S6.†

The electrical transport properties of $(Ge_{1-x-2y}Bi_xTe_{1-2y})(CuInTe_2)_y$ samples are given in Fig. 3. Fig. 3a shows that the electrical conductivity generally decreases with increasing temperature, indicating the degenerated semiconductor behaviour. But for y is $\geq$0.01, the electrical conductivity increases slightly at ~573 K. This is attributed to the valence band switch between L and Σ points induced by the second-order structural transition.[34,48] In addition, this could be explained by an attenuated band bending at the interface between GeTe and $CuInTe_2$, since the large Fermi level offset between the two materials at room temperature almost vanishes

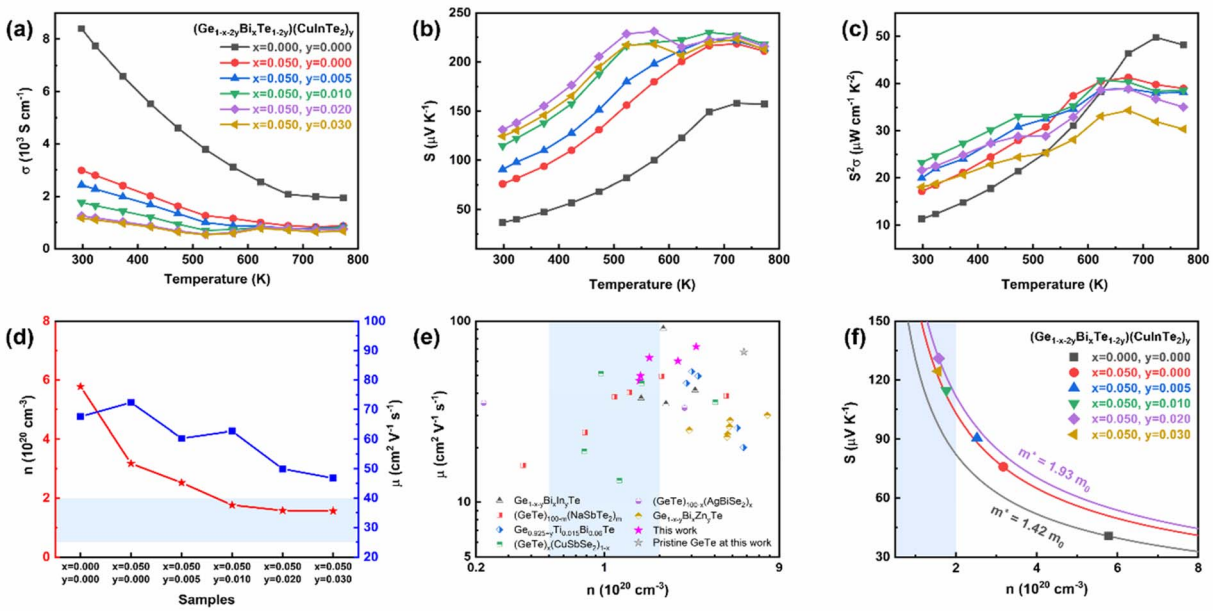

Fig. 3 Temperature-dependent (a) electrical conductivity, (b) Seebeck coefficient, and (c) power factor of $(Ge_{1-x-2y}Bi_xTe_{1-2y})(CuInTe_2)_y$ samples. (d) Composition-dependent Hall carrier concentration and Hall mobility at room temperature. Carrier concentration-dependent (e) Hall mobility in comparison with other reported data and (f) the Seebeck coefficient at room temperature.

at around ~600 K.[67] The intrinsically high Ge vacancies in pristine GeTe contribute to having a high electrical conductivity value of 8400 S cm^{-1} at room temperature as shown in Fig. 3a. With the doping of 5% Bi, the electrical conductivity decreases to 2984 S cm^{-1}, since Bi^{3+} effectively suppresses the Ge vacancies by providing an extra electron.[34,57,58,68] Further alloying of $CuInTe_2$ compounds, which have an intrinsically low carrier concentration (~10^{18} cm^{-3}),[50] reduces the hole carrier concentration, leading to a gradual decrease in electrical conductivity at room temperature to 1953 S cm^{-1}. Bi doping and $CuInTe_2$ alloying can maintain the optimal carrier concentration (0.5–2.0 × 10^{20} cm^{-3}) of GeTe-based materials from a doping content of $y = 0.01$, as depicted in Fig. 3d.[69] In addition, Fig. 3e shows that GeTe compounds in this work have relatively higher mobility compared with those in previous reports.[32,34,70–72] This can be elucidated by the reduced Ge vacancies and the similarity between the electronegativity of Ge and Cu.[48,73]

The Seebeck coefficient of $(Ge_{1-x-2y}Bi_xTe_{1-2y})(CuInTe_2)_y$ samples is shown in Fig. 3b. The positive value of the Seebeck coefficient manifests a p-type semiconductor with holes acting as the majority charge carriers. The Seebeck coefficient is considerably enhanced after Bi doping and $CuInTe_2$ alloying from ~36.7 μV K^{-1} to ~131 μV K^{-1} at room temperature. This is a result of the reduced carrier concentration (Fig. 3d) and the simultaneously increased effective mass (Fig. 3f). When the dopant composition is increased, the carrier concentration reaches an optimal level, and at the same time the effective mass increases due to changes in the electronic structure, including the hyperconvergence valence bands and the induced resonance level, as will be explained in the following section. The effective mass of $(Ge_{1-x-2y}Bi_xTe_{1-2y})(CuInTe_2)_y$ samples is presented in the Pisarenko plot calculated with the single parabolic band (SPB) model. The effective mass increases from 1.42 m_0 of pristine GeTe to 1.93 m_0 of the $(Ge_{0.91}Bi_{0.05}Te_{0.96})(CuInTe_2)_{0.02}$ sample, where m_0 is the electron mass. The temperature-dependent power factor is shown in Fig. 3c. Synergetically, an enhanced power factor of ~23 μW cm^{-1} K^{-2} is obtained at room temperature and ~41 μW cm^{-1} K^{-2} at 623 K in the $(Ge_{0.93}Bi_{0.05}Te_{0.98})(CuInTe_2)_{0.01}$ sample.

To better understand the improvement in the Seebeck coefficient of the multi-doped systems we compared the electronic structure of pristine GeTe with that of the multi-doped cubic system (Fig. 4a). We estimated a principal band gap of 0.26 eV at the Γ point in pristine GeTe due to the folding of the L point of the primitive cell Brillouin zone onto the Γ point of the supercell Brillouin zone.[74] An energy gap of 0.20 eV and 0.19 eV was also observed between the light (at the Γ point) and heavy (at the $Z + \delta$ point in the $Z \rightarrow R$ direction) carrier sub-bands in the conduction and valence band regions, respectively, preventing the contribution of the heavy carrier bands towards the transport properties. A heavy hole band was also seen at the $\Gamma + \delta'$ point in the $\Gamma \rightarrow X$ direction 0.06 eV below the valence band maximum. The partial density of states (pDOS) reveals that the valence band has a major contribution from the 'p' states of Te atoms and the conduction band, from the 'p' states of Ge atoms (Fig. 4b).

When Bi, In and Cu were doped simultaneously in GeTe we observe a very interesting electronic structure (Fig. 4c). Although we see a decrease in the energy gap at the Γ point by 0.1 eV in comparison to that of pristine GeTe, several favourable

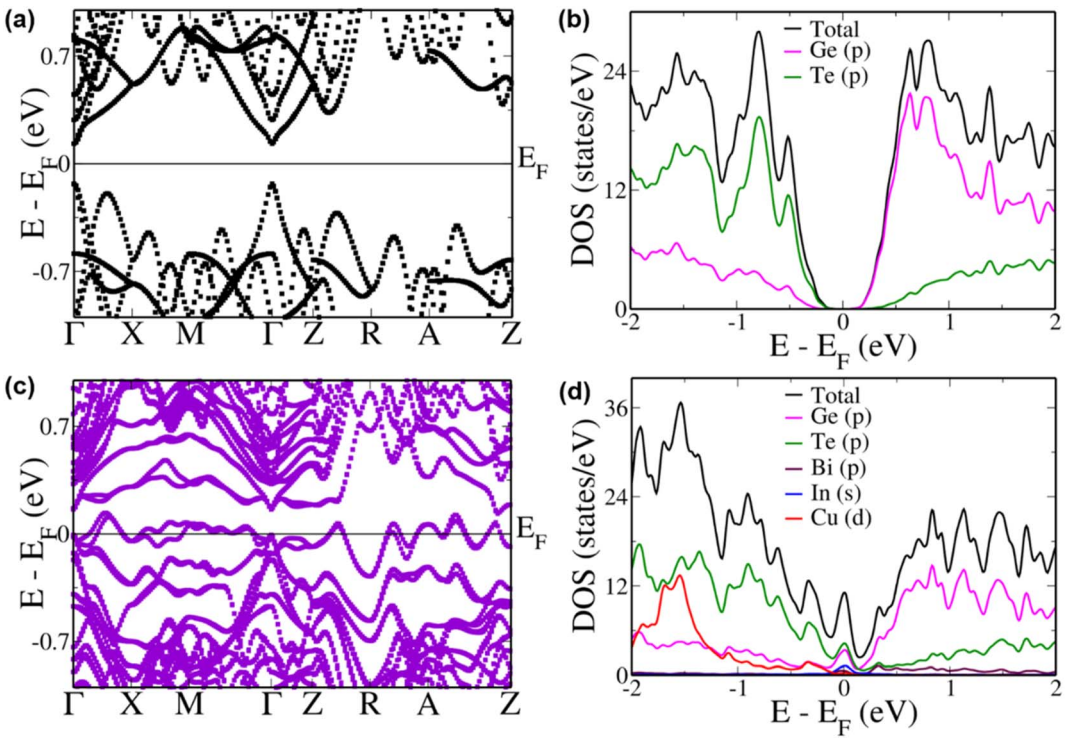

Fig. 4 Electronic structure and pDOS of cubic (a and b) $Ge_{16}Te_{16}$; (c and d) $Ge_{13}BiInCuTe_{16}$.

features appear near the Fermi level. The heavy hole sub-bands at the $Z + \delta$ point in the $Z \rightarrow$ R direction and the $\Gamma + \delta'$ point in the $\Gamma \rightarrow X$ direction increase in energy to an energy higher than that of the light hole valence sub-band at the Γ point. Such a phenomenon of hyperconvergence of valence sub-bands in GeTe-based materials was observed previously only in the case of Zn doping.[75] Even in the case of SnTe-based materials Zn was one of the dopants wherein such a feature of hyperconvergence of valence sub-bands was observed.[76–78] This indicates that the current combination of dopants is very unique and is able to tune the electronic structure similar to a Zn dopant but with additional features. Such a feature of hyperconvergence along with the introduction of resonance states has previously been known to cause a drastic increase in the Seebeck coefficient even at lower temperatures aiding in an increase in the overall ZT of the material.[76–78] The pDOS of this multi-doped GeTe composition shows a prominent increase in the DOS exactly at the Fermi level due to the hybridization of 's' orbitals of In along with the 'p' orbitals of Ge and Te atoms (Fig. 4d). Unlike the case of In resonance levels in SnTe where the resonance states are formed by the hybridization of the resonant dopant atomic orbital with the orbital of the anion, here we see the involvement of the cation orbitals as well.[79] This is further confirmed by analyzing the pDOS of In doped GeTe (Fig. S7†).

To study the contributions of individual dopants we analyzed the electronic structure of Bi, In and Cu doped GeTe separately (Fig. 5). In Bi doped GeTe, we see that the eight-fold degenerate conduction bands undergo splitting, and the lowermost doubly degenerate band touches the valence band maximum at the Γ point with 0.27 eV gap between the lowermost and the next set of conduction bands (Fig. 5a). The appearance of such resonance levels in GeTe due to Bi doping has been recently reported.[37] The energy offset between the light and heavy carrier bands also decreases to 0.11 eV and 0.17 eV between the Γ and $Z + \delta$ points in the $Z \rightarrow R$ direction in the conduction and valence band regions. Similarly, when In is doped in GeTe, the eight-fold degenerate bands split with the uppermost doubly degenerate bands touching the conduction band minimum with an energy gap of 0.25 eV between the split bands at the Γ point (Fig. 5b). Here, we observe an energy offset of 0.21 eV and 0.04 eV between the light and heavy carrier sub-bands in the conduction and valence band regions. The presence of resonance levels is confirmed in the DOS plot in the form of a prominent hump near the Fermi level (Fig. 5d). Doping of Cu in GeTe, on the other hand, decreases the principal band gap to 0.18 eV, with an increase in the valence band energy offset between the Γ point and the $Z + \delta$ point in the $Z \rightarrow$ R direction and the $\Gamma + \delta'$ point in the $\Gamma \rightarrow X$ direction to 0.25 eV and 0.07 eV (Fig. 5c). But it increases the energy of the bands at the M point leading to an energy difference of 0.17 eV from the valence band maximum at the Γ point compared to 0.45 eV in the case of pristine GeTe. Similarly, bands in the $R \rightarrow Z$ direction increase in energy with an energy difference of 0.15 eV between the $A + \delta''$ point in the $A \rightarrow Z$ direction and the valence band maximum at the Γ point. These features get more pronounced in the multi-doped GeTe, wherein the bands at the M point lie 0.08 eV above the valence band maximum at the Γ point and 0.162 eV at the $A + \delta''$ point in the $A \rightarrow Z$ direction revealing the impact of the right combination of dopants in aiding hyperconvergence. Similar features of the appearance of

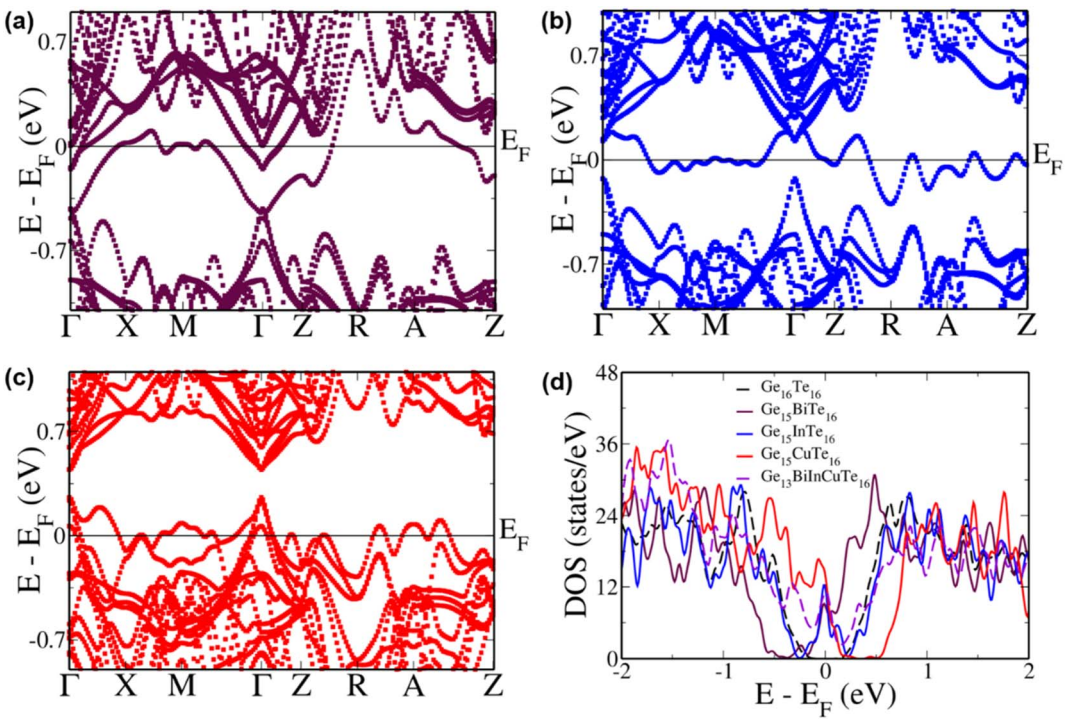

Fig. 5 Electronic structure of cubic (a) $Ge_{15}BiTe_{16}$; (b) $Ge_{15}InTe_{16}$; (c) $Ge_{15}CuTe_{16}$; (d) Total DOS of undoped and doped configurations.

resonance levels and hyperconvergence of valence sub-bands are observed in the electronic structure and pDOS of the rhombohedral phase of multi-doped GeTe in comparison to that of pristine GeTe (Fig. S8†).

Fig. 6a shows a plot of the temperature-dependent total thermal conductivity of $(Ge_{1-x-2y}Bi_xTe_{1-2y})(CuInTe_2)_y$ (x = 0, 0.05; y = 0, 0.005, 0.01, 0.02, and 0.03) samples. The total thermal conductivity of pristine GeTe decreases with increasing temperature until 673 K. Above 673 K, the total thermal conductivity increases because pristine GeTe undergoes a ferroelectric phase transition, accompanying the structural relaxation along the <111> direction.[34] With increasing x and y, the transition temperature decreases, indicating the expansion of the cubic structure region. Furthermore, the total thermal conductivity at room temperature significantly decreases from ~7.36 W m^{-1} K^{-1} of pristine GeTe to ~1.64 W m^{-1} K^{-1} of the $(Ge_{0.91}Bi_{0.05}Te_{0.96})(CuInTe_2)_{0.02}$ sample. This remarkable decrease is largely due to the decrease in electronic thermal conductivity (Fig. 6b) and partly due to the decrease in the lattice thermal conductivity (Fig. 6c). The reduction in electronic thermal conductivity is due to the reduced charge carrier concentration caused by the Bi doping and the $CuInTe_2$ alloying, which result in lower electrical conductivity.

The lattice thermal conductivity reduces from ~1.82 W m^{-1} K^{-1} of pristine GeTe to ~0.84 W m^{-1} K^{-1} of the $(Ge_{0.91}Bi_{0.05}Te_{0.96})(CuInTe_2)_{0.02}$ sample. A minimum lattice thermal conductivity of ~0.34 W m^{-1} K^{-1} is obtained at 623 K in the $(Ge_{0.93}Bi_{0.05}Te_{0.98})(CuInTe_2)_{0.01}$ sample, which is near the amorphous limit of ~0.33 W m^{-1} K^{-1}.[80] This decline in lattice thermal conductivity is ascribed to increased phonon scattering induced by point defects and phase boundaries, as shown in Fig. 2f, between the matrix and $CuInTe_2$ precipitate. Further insight is gained from the phonon frequency-dependent spectral lattice thermal conductivity shown in Fig. 6d calculated using the Debye–Callaway model,[81–83] which includes scattering by intrinsic normal (N) and Umklapp (U) processes as well as extrinsic scattering by grain boundaries (GB), point defects (PD), and $CuInTe_2$ nanoprecipitates (NP) after Bi doping and $CuInTe_2$ alloying. The detailed methods and parameters are presented in the ESI.† The spectral lattice thermal conductivity decreases with increasing point defects introduced by the various dopants, especially at a high f/f_D ratio, where f and f_D are the phonon and Debye phonon frequency, respectively. However, the effect of nano-precipitates appears to be dominant at a low f/f_D ratio and ineffective at a high f/f_D ratio. Unfortunately, the lattice thermal conductivity gradually increases when the doping composition is increased in the $(Ge_{0.91}Bi_{0.05}Te_{0.96})(CuInTe_2)_{0.02}$ and $(Ge_{0.89}Bi_{0.05}Te_{0.94})(CuInTe_2)_{0.03}$ samples. This abnormal increase is due to the increased size and density of $CuInTe_2$ precipitates (Fig. S2†) in the matrix and

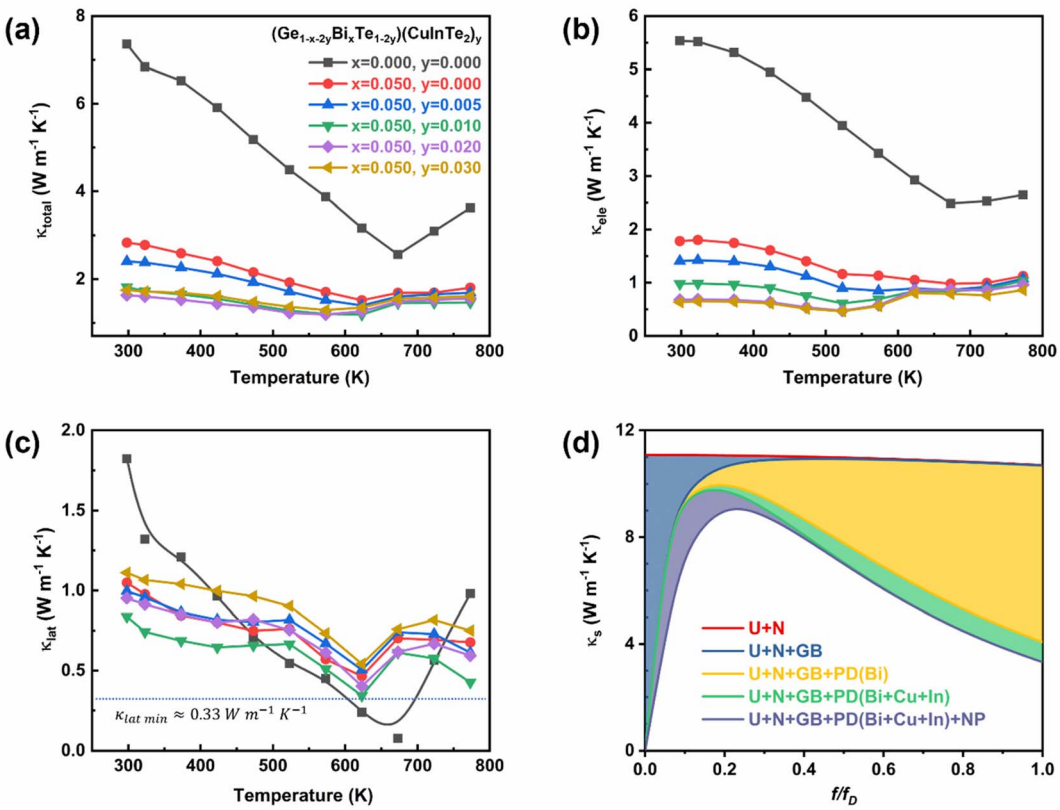

Fig. 6 Temperature-dependent (a) total thermal conductivity, (b) electronic thermal conductivity, and (c) lattice thermal conductivity of $(Ge_{1-x-2y}Bi_xTe_{1-2y})(CuInTe_2)_y$ samples. (d) Calculated spectral lattice thermal conductivity as a function of phonon frequency (f) based on various phonon scattering processes including the normal process (N), the Umklapp process (U), grain boundaries (GB), point defects (PD), and nanoprecipitate (NP) at 300 K.

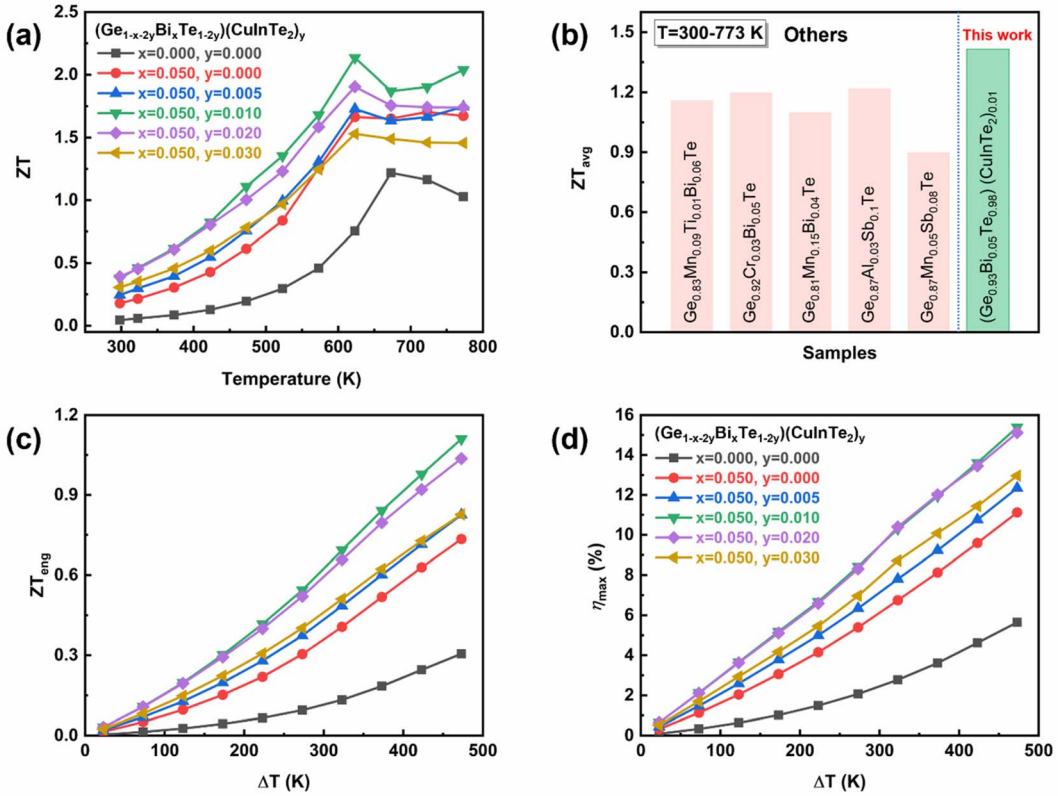

Fig. 7 (a) Temperature-dependent ZT of $(Ge_{1-x-2y}Bi_xTe_{1-2y})(CuInTe_2)_y$ samples and (b) the average ZT value with other reported GeTe compounds. (c) The ZT_{eng} values and (d) η_{max} values of $(Ge_{1-x-2y}Bi_xTe_{1-2y})(CuInTe_2)_y$ samples.

the difference in the κ_{latt} between the precipitates and the host's matrix. The κ_{latt} of $CuInTe_2$ ($\sim$6 W m^{-1} K^{-1}) is significantly higher than that of the $(Ge_{0.93}Bi_{0.05}Te_{0.98})(CuInTe_2)_{0.01}$ sample.[6,84,85]

Consequently, the peak ZT value of $\sim$2.16 at 623 K is obtained in the $(Ge_{0.93}Bi_{0.05}Te_{0.98})(CuInTe_2)_{0.01}$ sample as depicted in Fig. 7a, due to the comprehensive contribution of the optimized carrier concentration, hyperconverged electronic structure, and all-scale hierarchical phonon scattering by Bi doping and $CuInTe_2$ alloying. At room temperature, the $\sim$0.38 value of the $(Ge_{0.93}Bi_{0.05}Te_{0.98})(CuInTe_2)_{0.01}$ samples is almost 7 times higher than the $\sim$0.05 value of pristine GeTe. For practical applications as a thermoelectric device or module, a high average ZT (ZT_{avg}) over the entire operating temperature range is also essential. The ZT_{avg} is calculated by using $ZT_{avg} = Z\{(T_h + T_c)/2\}$ and ranges from 300 K to 773 K.[86] The obtained ZT_{avg} value $\sim$1.42 of the $(Ge_{0.93}Bi_{0.05}Te_{0.98})(CuInTe_2)_{0.01}$ is significantly higher than those of previously reported Pb-free GeTe compounds, as shown in Fig. 7b.[68,87–90] To more accurately predict the actual performance of a thermoelectric material at a given temperature difference, Fig. 7c and d indicate ZT_{eng} and $\eta_{max}(ZT_{eng})$ calculated by the method proposed by Kim *et al.*[86] for the $(Ge_{1-x-2y}Bi_xTe_{1-2y})(CuInTe_2)_y$ ($x = 0$, 0.05; $y = 0$, 0.005, 0.01, 0.02, and 0.03) samples, which are dependent on a temperature difference (ΔT), and T_c is fixed as 300 K in the calculation. For the temperature difference $\Delta T = 473$ K, the maximum ZT_{eng} of the $(Ge_{0.93}Bi_{0.05}Te_{0.98})(CuInTe_2)_{0.01}$ sample is calculated to be $\sim$1.1, which is an increase of $\sim$250% and $\sim$50% compared to $\sim$0.31 for pristine GeTe and $\sim$0.73 for $Ge_{0.95}Bi_{0.05}Te$, respectively. Moreover, $\eta_{max}(ZT_{eng})$ is predicted to be as high as $\sim$15.4% in the $(Ge_{0.93}Bi_{0.05}Te_{0.98})(CuInTe_2)_{0.01}$ sample for the temperature difference $\Delta T = 473$ K.

A thermoelectric material also requires sufficient mechanical stability. Vickers microhardness of the $(Ge_{1-x-2y}Bi_xTe_{1-2y})(CuInTe_2)_y$ ($x = 0$, 0.05; $y = 0$, 0.005, 0.01, 0.02, and 0.03) samples was measured and is depicted in Fig. 8a. Pristine GeTe exhibits a value as low as $\sim$134 Hv, similar to that previously reported, due to the high concentration of Ge vacancies.[8] $Ge_{0.95}Bi_{0.05}Te$ and $(Ge_{0.94}Bi_{0.05}Te_{0.99})(CuInTe_2)_{0.005}$ exhibit values of $\sim$193 Hv and of $\sim$195 Hv, respectively, whereas $(Ge_{0.93}Bi_{0.05}Te_{0.98})(CuInTe_2)_{0.01}$, $(Ge_{0.91}Bi_{0.05}Te_{0.96})(CuInTe_2)_{0.02}$ and $(Ge_{0.89}Bi_{0.05}Te_{0.91})(CuInTe_2)_{0.03}$ achieve very high values of $\sim$230 Hv, $\sim$277 Hv, and $\sim$268 Hv, respectively. The improved mechanical strength is due to the dense point defects, the optimally reduced Ge vacancy concentration (Fig. 3d), and the strain induced by dislocations and $CuInTe_2$ nanostructures (Fig. 2d, g, and h) with increasing dopant concentration. Fig. 8b shows the Hv values of our pristine GeTe and the $(Ge_{0.91}Bi_{0.05}Te_{0.96})(CuInTe_2)_{0.02}$ sample compared with the previously reported values of GeTe compounds,[34,80,91,92] and it can be seen that the $(Ge_{0.91}Bi_{0.05}Te_{0.96})(CuInTe_2)_{0.02}$ sample value is super high.

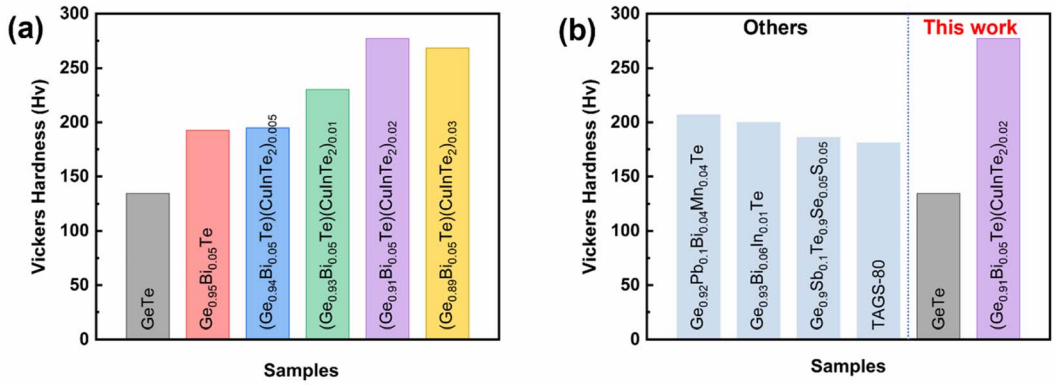

Fig. 8 (a) Vickers hardness values of $(Ge_{1-x-2y}Bi_xTe_{1-2y})(CuInTe_2)_y$ samples and (b) compared with those of other reported GeTe samples.

Conclusions

In this study, the simultaneous addition of Bi and $CuInTe_2$ to GeTe successfully adjusts the carrier concentration to an optimal level. The electronic structure calculations reveal the possibility of hyperconverged valence sub-bands and induced resonance levels. As the Seebeck coefficient increased, the power factor starts at ~23 μW cm^{-1} K^{-2} at room temperature and peaks at 623 K with a value of ~41 μW cm^{-1} K^{-2} in the $(Ge_{0.93}Bi_{0.05}Te_{0.98})(CuInTe_2)_{0.01}$ sample. The lattice thermal conductivity also decreased towards the amorphous limit. As a result, a peak ZT of ~2.16 at 623 K and a ZT_{avg} of ~1.42 from 300 K to 773 K were obtained in the $(Ge_{0.93}Bi_{0.05}Te_{0.98})(CuInTe_2)_{0.01}$ sample. A record high Vickers hardness value of ~277 Hv was obtained in the $(Ge_{0.91}Bi_{0.05}Te_{0.96})(CuInTe_2)_{0.02}$ sample.

Conflicts of interest

The authors declare no conflicts of financial interest.

Acknowledgements

This work was supported by grants from the National Research Foundation (NRF) of Korea (No. 2021R1A4A2001658 and 2022R1A2C1006790), and funded by the Korean government (MSIT). The author (USS) also acknowledges the grant from Science and Engineering Board, Department of Science and Technology, Government of India (SB/SRS/2021-22/73/CS) under the SERB Research Scientist scheme.

References

1 J. N. Kahiu, U. S. Shenoy, S. K. Kihoi, H. Kim, S. Yi, D. K. Bhat and H. S. Lee, *J. Alloys Compd.*, 2022, **891**, 162033.
2 M. Rakshit, D. Jana and D. Banerjee, *J. Mater. Chem. A*, 2022, **10**, 6872–6926.
3 Q. Wang, X. Xie, S. Li, Z. Zhang, X. Li, H. Yao, C. Chen, F. Cao, J. Sui, X. Liu and Q. Zhang, *J. Materiomics*, 2021, **7**, 756–765.
4 X. Yang, C. Wang, R. Lu, Y. Shen, H. Zhao, J. Li, R. Li, L. Zhang, H. Chen, T. Zhang and X. Zheng, *Nano Energy*, 2022, **101**, 107553.
5 S. K. Kihoi, J. N. Kahiu, H. Kim, U. S. Shenoy, D. K. Bhat, S. Yi and H. S. Lee, *J. Mater. Sci.: Mater. Electron.*, 2021, **85**, 76–86.
6 H. Kim, S. K. Kihoi and H. S. Lee, *J. Alloys Compd.*, 2021, **869**, 159381.
7 G. Tan, L. D. Zhao and M. G. Kanatzidis, *Chem. Rev.*, 2016, **116**, 12123–12149.
8 W. Di Liu, D. Z. Wang, Q. Liu, W. Zhou, Z. Shao and Z. G. Chen, *Adv. Energy Mater.*, 2020, **10**, 1–24.
9 L. E. Bell, *Science*, 2008, **321**, 1457–1461.
10 X. Li, J. Liu, S. Li, J. Zhang, D. Li, R. Xu, Q. Zhang, X. Zhang, B. Xu, Y. Zhang, F. Xu and G. Tang, *Nano Energy*, 2020, **67**, 104261.
11 Y. Pei, X. Shi, A. Lalonde, H. Wang, L. Chen and G. J. Snyder, *Nature*, 2011, **473**, 66–69.
12 S. K. Kihoi, U. S. Shenoy, D. K. Bhat and H. S. Lee, *J. Mater. Chem. C*, 2021, **9**, 9922–9931.
13 J. P. Heremans, V. Jovovic, E. S. Toberer, A. Saramat, K. Kurosaki, A. Charoenphakdee, S. Yamanaka and G. J. Snyder, *Science*, 2008, **321**, 1457–1461.
14 B. Paul, A. Kumar V. and P. Banerji, *J. Appl. Phys.*, 2010, **108**, 064322.
15 C. Gayner and Y. Amouyal, *Adv. Funct. Mater.*, 2020, **30**, 1–17.
16 Y. L. Pei, H. Wu, D. Wu, F. Zheng and J. He, *J. Am. Chem. Soc.*, 2014, **136**, 13902–13908.
17 T. Berry, C. Fu, G. Auffermann, G. H. Fecher, W. Schnelle, F. Serrano-Sanchez, Y. Yue, H. Liang and C. Felser, *Chem. Mater.*, 2017, **29**, 7042–7048.
18 B. Jiang, Y. Yu, J. Cui, X. Liu, L. Xie, J. Liao, Q. Zhang, Y. Huang, S. Ning, B. Jia, B. Zhu, S. Bai, L. Chen, S. J. Pennycook and J. He, *Science*, 2021, **371**, 830–834.
19 K. Biswas, J. He, I. D. Blum, C. I. Wu, T. P. Hogan, D. N. Seidman, V. P. Dravid and M. G. Kanatzidis, *Nature*, 2012, **489**, 414–418.
20 Y. Luo, J. Yang, Q. Jiang, W. Li, Y. Xiao, L. Fu, D. Zhang, Z. Zhou and Y. Cheng, *Nano Energy*, 2015, **18**, 37–46.
21 W. Li, Y. Luo, Y. Zheng, C. Du, Q. Liang, B. Zhu and L. Zhao, *J. Mater. Sci. Technol.*, 2018, **29**, 4732–4737.
22 J. He, S. N. Girard, J. C. Zheng, L. Zhao, M. G. Kanatzidis and V. P. Dravid, *Adv. Mater.*, 2012, **24**, 4440–4444.
23 L. Hu, T. Zhu, X. Liu and X. Zhao, *Adv. Funct. Mater.*, 2014, **24**, 5211–5218.

24 Y. Yu, M. Cagnoni, O. Cojocaru-Mirédin and M. Wuttig, *Adv. Funct. Mater.*, 2012, **24**, 4440–4444.
25 N. Mingo, D. Hauser, N. P. Kobayashi, M. Plissonnier and A. Shakouri, *Nano Lett.*, 2009, **9**, 711–715.
26 T. Zhu, C. Fu, H. Xie, Y. Liu and X. Zhao, *Adv. Energy Mater.*, 2015, **5**, 1–13.
27 F. Gascoin, S. Ottensmann, D. Stark, S. M. Haïle and G. J. Snyder, *Adv. Funct. Mater.*, 2005, **15**, 1860–1864.
28 M. Rull-Bravo, A. Moure, J. F. Fernández and M. Martín-González, *RSC Adv.*, 2015, **5**, 41653–41667.
29 S. Zhi, J. Li, L. Hu, J. Li, N. Li, H. Wu, F. Liu, C. Zhang, W. Ao, H. Xie, X. Zhao, S. J. Pennycook and T. Zhu, *Adv. Sci.*, 2021, **8**, 1–10.
30 M. Hong, W. Lyv, M. Li, S. Xu, Q. Sun, J. Zou and Z. G. Chen, *Joule*, 2020, **4**, 2030–2043.
31 Y. F. Tsai, M. Y. Ho, P. C. Wei and H. J. Wu, *Acta Mater.*, 2022, **222**, 117406.
32 S. Duan, W. Xue, H. Yao, X. Wang, C. Wang, S. Li, Z. Zhang, L. Yin, X. Bao, L. Huang, X. Wang, C. Chen, J. Sui, Y. Chen, J. Mao, F. Cao, Y. Wang and Q. Zhang, *Adv. Energy Mater.*, 2022, **12**, 1–8.
33 M. Li, Q. Sun, S. D. Xu, M. Hong, W. Y. Lyu, J. X. Liu, Y. Wang, M. Dargusch, J. Zou and Z. G. Chen, *Adv. Mater.*, 2021, **33**, 1–8.
34 S. Perumal, M. Samanta, T. Ghosh, U. S. Shenoy, A. K. Bohra, S. Bhattacharya, A. Singh, U. V. Waghmare and K. Biswas, *Joule*, 2019, **3**, 2565–2580.
35 J. P. Gaspard, *C. R. Phys.*, 2016, **17**, 389–405.
36 J. Li, X. Zhang, Z. Chen, S. Lin, W. Li, J. Shen, I. T. Witting, A. Faghaninia, Y. Chen, A. Jain, L. Chen, G. J. Snyder and Y. Pei, *Joule*, 2018, **2**, 976–987.
37 U. S. Shenoy, K. D. Goutham and D. K. Bhat, *J. Alloys Compd.*, 2022, **921**, 165965.
38 A. Manchon, H. C. Koo, J. Nitta, S. M. Frolov and R. A. Duine, *Nat. Mater.*, 2015, **14**, 871–882.
39 T. Xing, C. Zhu, Q. Song, H. Huang, J. Xiao, D. Ren, M. Shi, P. Qiu, X. Shi, F. Xu and L. Chen, *Adv. Mater.*, 2021, 2008773.
40 X. Wang, W. Xue, Z. Zhang, X. Li, L. Yin, C. Chen, B. Yu, J. Sui, F. Cao, X. Liu, J. Mao, Y. Wang, X. Lin and Q. Zhang, *ACS Appl. Mater. Interfaces*, 2021, **13**, 45717–45725.
41 K. S. Bayikadi, C. T. Wu, L. C. Chen, K. H. Chen, F. C. Chou and R. Sankar, *J. Mater. Chem. A*, 2020, **8**, 5332–5341.
42 L. Wu, X. Li, S. Wang, T. Zhang, J. Yang, W. Zhang, L. Chen and J. Yang, *NPG Asia Mater.*, 2017, **9**, 1–7.
43 Y. Jin, Y. Xiao, D. Wang, Z. Huang, Y. Qiu and L. D. Zhao, *ACS Appl. Energy Mater.*, 2019, **2**, 7594–7601.
44 M. Hong, Y. Wang, T. Feng, Q. Sun, S. Xu, S. Matsumura, S. T. Pantelides, J. Zou and Z. G. Chen, *J. Am. Chem. Soc.*, 2019, **141**, 1742–1748.
45 B. Jiang, W. Wang, S. Liu, Y. Wang, C. Wang, Y. Chen, L. Xie, M. Huang and J. He, *Science*, 2022, **377**, 208–213.
46 S. H. Yang, T. J. Zhu, T. Sun, J. He, S. N. Zhang and X. B. Zhao, *Nanotechnology*, 2008, **19**, 245707.
47 N. Li, W. He, C. Li, G. Wang, G. Wang, X. Zhou and X. Lu, *J. Mater. Chem. A*, 2021, **9**, 2385–2393.
48 Q. Zhang, Z. Ti, Y. Zhu, Y. Zhang, Y. Cao, S. Li, M. Wang, D. Li, B. Zou, Y. Hou, P. Wang and G. Tang, *ACS Nano*, 2021, **15**, 19345–19356.
49 H. Kim, C. O. Park, H. Jeong, S. K. Kihoi, S. Yi, H. S. Kim, K. H. Lee and H. S. Lee, *Inorg. Chem. Front.*, 2021, **8**, 2782–2787.
50 Y. Luo, J. Yang, Q. Jiang, W. Li, D. Zhang, Z. Zhou, Y. Cheng, Y. Ren and X. He, *Adv. Energy Mater.*, 2016, **6**, 1600007.
51 A. Kosuga, K. Umekage, M. Matsuzawa, Y. Sakamoto and I. Yamada, *Inorg. Chem.*, 2014, **53**, 6844–6849.
52 H. S. Kim, Z. M. Gibbs, Y. Tang, H. Wang and G. J. Snyder, *APL Mater.*, 2015, **3**, 1–6.
53 P. Giannozzi, S. Baroni, N. Bonini, M. Calandra, R. Car, C. Cavazzoni, D. Ceresoli, G. L. Chiarotti, M. Cococcioni, I. Dabo, A. Dal Corso, S. De Gironcoli, S. Fabris, G. Fratesi, R. Gebauer, U. Gerstmann, C. Gougoussis, A. Kokalj, M. Lazzeri, L. Martin-Samos, N. Marzari, F. Mauri, R. Mazzarello, S. Paolini, A. Pasquarello, L. Paulatto, C. Sbraccia, S. Scandolo, G. Sclauzero, A. P. Seitsonen, A. Smogunov, P. Umari and R. M. Wentzcovitch, *J. Phys.: Condens. Matter*, 2009, **21**, 395502.
54 J. P. Perdew, K. Burke and M. Ernzerhof, *Phys. Rev. Lett.*, 1996, **77**, 3865–3868.
55 R. Zhang, J. Pei, Z. Shan, W. Zhou, Y. Wu, Z. Han, Y. H. Zhao, J. F. Li, Z. H. Ge and B. P. Zhang, *Chem. Eng. J.*, 2022, **429**, 132275.
56 J. Li, Z. Chen, X. Zhang, H. Yu, Z. Wu, H. Xie, Y. Chen and Y. Pei, *Adv. Sci.*, 2017, **4**, 1700341.
57 H. Jeong, S. K. Kihoi, H. Kim and H. S. Lee, *J. Mater. Res. Technol.*, 2021, **15**, 6312–6318.
58 S. Perumal, P. Bellare, U. S. Shenoy, U. V. Waghmare and K. Biswas, *Chem. Mater.*, 2017, **29**, 10426–10435.
59 C. Zhu, J. Wang, F. Luo, S. Zhang, J. Wang, Y. Zhang, H. Liu and Z. Sun, *ACS Appl. Mater. Interfaces*, 2022, **14**, 38854–38864.
60 S. Perumal, S. Roychowdhury, D. S. Negi, R. Datta and K. Biswas, *Chem. Mater.*, 2015, **27**, 7171–7178.
61 A. S. Frolov, J. Sánchez-Barriga, C. Callaert, J. Hadermann, A. V. Fedorov, D. Y. Usachov, A. N. Chaika, B. C. Walls, K. Zhussupbekov, I. V. Shvets, M. Muntwiler, M. Amati, L. Gregoratti, A. Y. Varykhalov, O. Rader and L. V. Yashina, *ACS Nano*, 2020, **14**, 16576–16589.
62 M. Snykers, P. Delavignette and S. Amelinckx, *Mater. Res. Bull.*, 1972, **7**, 831–839.
63 H. S. Lee, B. S. Kim, C. W. Cho, M. W. Oh, B. K. Min, S. D. Park and H. W. Lee, *Acta Mater.*, 2015, **91**, 83–90.
64 D. Wu, L. D. Zhao, S. Hao, Q. Jiang, F. Zheng, J. W. Doak, H. Wu, H. Chi, Y. Gelbstein, C. Uher, C. Wolverton, M. Kanatzidis and J. He, *J. Am. Chem. Soc.*, 2014, **136**, 11412–11419.
65 H. Wu, F. Zheng, D. Wu, Z. H. Ge, X. Liu and J. He, *Nano Energy*, 2015, **13**, 626–650.
66 M. J. Hÿtch, E. Snoeck and R. Kilaas, *Ultramicroscopy*, 1998, **74**, 131–146.
67 S. Hui, W. Gao, X. Lu, A. Panda, T. P. Bailey, A. A. Page, S. R. Forrest, D. T. Morelli, X. Pan, K. P. Pipe and C. Uher, *Adv. Energy Mater.*, 2018, **8**, 1–8.

68 Z. Liu, J. Sun, J. Mao, H. Zhu, W. Ren, J. Zhou, Z. Wang, D. J. Singh, J. Sui, C. W. Chu and Z. Ren, *Proc. Natl. Acad. Sci. U. S. A.*, 2018, **115**, 5332–5337.
69 Z. Bu, W. Li, J. Li, X. Zhang, J. Mao, Y. Chen and Y. Pei, *Mater. Today Phys.*, 2019, **9**, 1–7.
70 C. Zhu, F. Luo, J. Wang, S. Zhang, J. Wang, H. Liu and Z. Sun, *J. Mater. Chem. C*, 2022, **14**, 9052–9061.
71 N. Man, J. Cai, Z. Guo, G. Liu, P. Sun, H. Wang, Q. Zhang, X. Tan, Y. Yin and J. Jiang, *ACS Appl. Energy Mater.*, 2021, **4**, 4242–4247.
72 M. Samanta, T. Ghosh, R. Arora, U. V. Waghmare and K. Biswas, *J. Am. Chem. Soc.*, 2019, **141**, 19505–19512.
73 L. C. Yin, W. Di Liu, M. Li, Q. Sun, H. Gao, D. Z. Wang, H. Wu, Y. F. Wang, X. L. Shi, Q. Liu and Z. G. Chen, *Adv. Energy Mater.*, 2021, **11**, 1–8.
74 D. K. Bhat and U. S. Shenoy, *J. Alloys Compd.*, 2020, **843**, 155989.
75 D. K. Bhat and U. S. Shenoy, *New J. Chem.*, 2020, **44**, 17664–17670.
76 U. S. Shenoy and D. K. Bhat, *J. Mater. Chem. C*, 2020, **8**, 2036–2042.
77 D. K. Bhat and U. S. Shenoy, *J. Alloys Compd.*, 2020, **834**, 155181.
78 U. S. Shenoy and D. K. Bhat, *J. Alloys Compd.*, 2022, **892**, 162221.
79 U. S. Shenoy and D. K. Bhat, *J. Mater. Chem. C*, 2019, **7**, 4817–4821.
80 D. Z. Wang, W. Di Liu, M. Li, L. C. Yin, H. Gao, Q. Sun, H. Wu, Y. Wang, X. L. Shi, X. Yang, Q. Liu and Z. G. Chen, *Chem. Eng. J.*, 2022, **441**, 136131.
81 J. Callaway and H. C. Von Baeyer, *Phys. Rev.*, 1960, **120**, 1149–1154.
82 D. Bessas, I. Sergueev, H. C. Wille, J. Peron, D. Ebling and R. P. Hermann, *Phys. Rev. B: Condens. Matter Mater. Phys.*, 2012, **86**, 1–9.
83 M. Hong, T. C. Chasapis, Z. G. Chen, L. Yang, M. G. Kanatzidis, G. J. Snyder and J. Zou, *ACS Nano*, 2016, **10**, 4719–4727.
84 Y. M. Zhou, H. J. Wu, Y. L. Pei, C. Chang, Y. Xiao, X. Zhang, S. K. Gong, J. Q. He and L. D. Zhao, *Acta Mater.*, 2017, **125**, 542–549.
85 X. L. Shi, J. Zou and Z. G. Chen, *Chem. Rev.*, 2020, **120**, 7399–7515.
86 H. S. Kim, W. Liu, G. Chen, C. W. Chu and Z. Ren, *Proc. Natl. Acad. Sci. U. S. A.*, 2015, **112**, 8205–8210.
87 A. Kumar, P. Bhumla, T. Parashchuk, S. Baran, S. Bhattacharya and K. T. Wojciechowski, *Chem. Mater.*, 2021, **33**, 3611–3620.
88 C. Xu, Z. Liang, W. Ren, S. Song, F. Zhang and Z. Ren, *Adv. Energy Mater.*, 2022, **12**, 2202392.
89 Y. Dou, J. Li, Y. Xie, X. Wu, L. Hu, F. Liu, W. Ao, Y. Liu and C. Zhang, *Mater. Today Phys.*, 2021, **20**, 100497.
90 J. Shuai, Y. Sun, X. Tan and T. Mori, *Small*, 2020, **16**, 1906921.
91 M. Samanta and K. Biswas, *J. Am. Chem. Soc.*, 2017, **139**, 9382–9391.
92 J. Davidow and Y. Gelbstein, *J. Electron. Mater.*, 2013, **42**, 1542–1549.

